Precipitation Uncertainty Due to Variations in Precipitation Particle Parameters within a Simple Microphysics Scheme

MATTHEW S. GILMORE

NOAA/National Severe Storms Laboratory, and Cooperative Institute for Mesoscale Meteorological Studies, University of Oklahoma, Norman, Oklahoma

JERRY M. STRAKA

School of Meteorology, University of Oklahoma, Norman, Oklahoma

ERIK N. RASMUSSEN

NOAA/National Severe Storms Laboratory, and Cooperative Institute for Mesoscale Meteorological Studies, University of Oklahoma, Norman, Oklahoma

(Manuscript received and in final form 8 March 2004)

ABSTRACT

This work reports on the sensitivity of accumulated precipitation to the microphysical parameterization in simulations of deep convective storms using a three-dimensional, nonhydrostatic cloud model with a simple liquid–ice microphysics scheme. Various intercept parameters from an assumed Marshall–Palmer exponential size distribution are tested along with two particle densities for the hail/graupel (qh) category. These variations allow testing of unique qh distributions that have been observed and documented in previous literature. Tests are conducted for a single thermodynamic profile and three idealized wind shear profiles.

The amount of accumulated precipitation at the ground is very sensitive to the way the qh category is parameterized. Distributions characterized by larger intercepts and/or smaller particle density have a smaller mass-weighted mean terminal fall velocity and produce smaller qh mixing ratios spread over a larger area. For example, for a qh category weighted toward graupel, only a fourth as much precipitation accumulates on the ground over 2 h (and none is hail) compared to a qh category weighted toward large hail (with baseball-sized stones common).

The inherent uncertainty within the qh distribution for this simple cloud-scale three-class ice microphysics scheme suggests limited usefulness in the forecasting of ground-accumulated precipitation and damaging hail.

1. Introduction

In order to improve warm-season flood forecasting, efforts are under way to couple rainfall output from cloud-scale atmospheric models to hydrological models. However, before such efforts can bear fruit, the variation in rainfall due to the uncertainties inherent in the cloud-scale microphysical parameterizations must be assessed. Understanding these microphysical sensitivities is one important problem in the forecasting of precipitation (Droegemeier et al. 2000). Assessing these sensitivities is also important before such models can be used to reliably forecast damaging hail events.

Explicit cloud-scale forecast models routinely use microphysics schemes that include the ice phase. For instance, the Advanced Regional Prediction System (ARPS; Xue et al. 2001), the Weather Research and Forecasting model (WRF; Michalakes et al. 2001), and the Regional Atmospheric Modeling System (RAMS; Walko et al. 1995) all include simple microphysics packages that represent between three and five categories of ice along with the liquid phase. The single-moment schemes with three ice classes are very similar to that presented by Lin et al. (1983, hereafter LFO83). LFO83-like schemes have been used in numerous cloud modeling studies (e.g., LFO83 Fovell and Ogura 1988; Tao and Simpson 1989, 1993; McCumber et al. 1991; Ferrier et al. 1995; Liu et al. 1997; Xue et al. 2001).

Previous studies have shown that the characteristics of the different ice hydrometeors used in cloud-scale simulations of thunderstorms can greatly influence precipitation distribution, its fallout (e.g., Cotton et al. 1982; McCumber et al. 1991; Ferrier et al. 1995), and the resulting downdraft intensity (e.g., Proctor 1988, 1989; Straka and Anderson 1993). For example, larger

Corresponding author address: Dr. Matthew S. Gilmore, University of Illinois at Urbana–Champaign, Dept. of Atmospheric Sciences, 105 S. Gregory St., Urbana, IL 61801.
E-mail: gilmore@atmos.uiuc.edu

particles such as hail can fall much more quickly than rain, while snow falls more slowly. Bennetts and Rawlins (1981) suggested that higher fall speeds of hail modulate the precipitation distribution in the low levels, resulting in earlier surface rainfall. Additionally, Fovell and Ogura (1988) found that melting hail/graupel was the largest source of rainwater in 2D midlatitude squall-line simulations. Consistent with these studies, Gilmore et al. (2004, hereafter GSR2004) found that the inclusion of a fast-falling hail/graupel species resulted in enhanced low-level rain production and greater ground-accumulated rainfall below simulated supercell and multicell storms.

Thus, hail/graupel may be a particularly important species that influences the quantity and type of precipitation received at the ground in many types of midlatitude thunderstorms. Our study focuses on supercell environments with large instability and wind shear (often veering). Supercells seem to be associated with the most damaging hailstorms (e.g., Changnon 2001) and, sometimes, extreme rainfall and flooding (Smith et al. 2001). We are also interested in hail production within less organized but apparently more common multicells.

Hail damage is not simply a function of hail size. While roof destruction increases with hailstone size (Collins and Howe 1964; Changnon 1977; Marshall et al. 2002), hailstones of only 6-mm diameter can damage crops such as corn, wheat, tobacco, and tea, especially when the cumulative hail mass is large (Changnon 1971, 1977, 1999). Of course, unsheltered livestock and people are particularly vulnerable to large hail. Understanding how the parameterized hail/graupel species influences hailstone size and mass in simulated storms is important before that output is used as guidance in storm-scale forecasts.

Therefore, the impact of the uncertainties inherent in the parameters defining the hail/graupel distribution are studied first. We later show that there is less ground-accumulated precipitation sensitivity due to uncertainties in the parameters describing rain and snow distributions.

In section 2 of this paper, we briefly describe the microphysics scheme and its limitations that form the basis of this sensitivity study. A complete description of the microphysics scheme can be found in the peer-reviewed supplement to GSR2004 (this electronic supplement is available at the Journals Online Web site: http://dx.doi.org/10.1175/MWR2760.s1). In section 3, we introduce the numerical cloud model and experimental procedure. The results are reported and briefly discussed in section 4. Implications for precipitation forecasting and applicability of the results for other environments are among the topics discussed in section 5. The paper is concluded in section 6.

2. Microphysics description

The simple liquid–ice microphysics scheme used herein is referred to as 3-ICE. (In GSR2004 this scheme was referred to as ''Li.'') 3-ICE was chosen primarily because of its similarity to the LFO83-like schemes that are currently used in storm-scale forecast models such as ARPS, WRF, and RAMS. The purpose of using a simple microphysics scheme is to demonstrate some of its limitations and motivate the use of more sophisticated schemes.

3-ICE predicts a single-moment bulk mixing ratio for each precipitating class. The smaller particles (cloud ice and cloud water, hereafter qi and qw, respectively) are monodisperse. The faster-precipitating particles (rain, snow, and hail/graupel, hereafter qr, qs, and qh, respectively) are defined by Marshall–Palmer exponential size distributions (Marshall and Palmer 1948):

$$n_x(D) = n_{\mathrm{ox}} \exp(-D_x D_{\mathrm{nx}}^{-1}), \tag{1}$$

where x is r (rain), s (snow), or h (hail), and $n_x(D)\delta D$ is the number of drops per unit volume (number concentration) between diameters D and $D + \delta D$. The exponential size distribution assumption appears to provide a good fit to actual rain and snow distributions ($D > 1$ mm) and hail distributions ($D > 5$ mm) (e.g., Marshall and Palmer 1948; Gunn and Marshall 1958; Pruppacher and Klett 1978; Cheng et al. 1985; Braham 1990). Higher-order gamma functions, as used in RAMS, can be used to provide more realistic distributions at smaller diameters (Walko et al. 1995); however, the current work follows the exponential form commonly used in ARPS and WRF. The intercept parameter, n_{ox}, is the value of $n_x(D)$ for $D = 0$. The mean size diameter of an exponential distribution, D_{nx} is equal to the inverse of the slope parameter. Here D_{nx} is diagnosed[1] using

$$D_{\mathrm{nx}} = [\rho q_x/(\pi \rho_x n_{\mathrm{ox}})]^{1/4}, \tag{2}$$

where ρ_x is the species particle density (constant), ρ is the local air density, and q_x is the species mixing ratio (e.g., Kessler 1969; Smith et al. 1975). Thus, each exponential particle distribution is a function of ρ_x and n_o. For a given q_x, if n_{ox} or ρ_x are decreased, the distribution becomes more heavily weighted toward larger-sized particles.

In actual hailstorms, the internal structure of the riming hail/graupel (which determines particle density) is a function of the impact velocity, water drop size, air temperature, and particle temperature (Macklin 1961; Macklin and Ryan 1962, 1965; Pflaum and Pruppacher 1979). As reviewed by LFO83, the water density can vary within a single hailstone or graupel particle. Therefore, what is reported is usually the *net* or *bulk* particle density for a single stone. Depending upon the individual growth trajectories (e.g., Miller et al. 1988), there can be a great diversity of bulk particle density throughout the storm (Pruppacher and Klett 1978), and this is reported in Table 1. Also, the n_{oh} (intercept for the qh

[1] Alternatively, as in RAMS, the D_{nx} can be set to a constant and the n_{ox} diagnosed.

TABLE 1. A summary of thunderstorm hail and graupel bulk particle densities observed in situ or at the ground. The term ''graupel'' and ''hail,'' per convention, are used to describe any particle less than or greater than 5 mm in equivalent spherical diameter, respectively, regardless of bulk particle density or number concentration.

Observed ρ_h (kg m^{-3})	Species	References
700–900	Hail	Pruppacher and Klett (1978)
400	Hail	D. Zrnić (2001, personal communication)
50–890	Graupel	Pruppacher and Klett (1978)

TABLE 2. A summary of thunderstorm hail and graupel intercept parameters observed in situ or at the ground. Note that the units dm^{-3} mm^{-1} are equivalent to m^{-4}.

Observed n_{oh} (dm^{-3} mm^{-1})	Species	References
10^3–10^5	Hail	Dennis et al. (1971); Federer and Waldvogel (1975); Spahn (1976)
10^2–10^6	Hail	Cheng et al. (1985)
10^4–10^8	Hail/graupel (>1 mm)	Knight et al. (1982)
10^6–10^{10}	Graupel (<1 mm)	Knight et al. (1982)

distribution) can vary widely within and among hailstorms (Dennis et al. 1971; Federer and Waldvogel 1975; Spahn 1976; Knight et al. 1982; Ziegler et al. 1983; Cheng et al. 1985). These n_{oh} observations (not necessarily from supercells) are summarized in Table 2 and Fig. 1. Hailstorm n_{oh} in the literature ranges from 10^2 to greater than 10^8 m^{-4} (Table 2).

The consequences of prescribing a constant n_{ox} and ρ_x are the focus of our current investigation. These constants represent a limitation of single-moment bulk microphysics schemes that predict mixing ratio only (such as LFO83 and 3-ICE). However, these are not the only limitations to such schemes.

Two other artifacts may also affect the microphysics but are not investigated here. One is the mass-weighted mean terminal fall velocity (hereafter abbreviated as simply ''fall velocity'') that is evaluated at each grid volume. It is applied uniformly to each particle in the precipitation particle spectrum—forcing the smaller (larger) particles to fall too quickly (slowly). Furthermore, there are a variety of observational studies to justify different constants in the fallout equations and that can affect fallout and accretion rates between species (e.g., McFarquhar and Black 2004). Another artifact, which an anonymous reviewer suggested we mention, is that collection efficiencies are often assumed invariant with particle diameter (e.g., Farley and Orville 1986; Orville and Kopp 1977; LFO83; GSR2004). The efficiency assumption ignores the strong dependence upon particle diameter and shape for two interacting distributions (e.g., Pruppacher and Klett 1978). Particularly in the case of the efficiencies, there could be a great deal of microphysical uncertainty, and future work is needed to understand any resulting precipitation sensitivities.

3. Experimental design

a. Model and domain parameters

The Straka Atmospheric Model [SAM; Johnson et al. (1993, 1994); Straka and Anderson (1993); Carpenter et al. (1998)] is the three-dimensional, nonhydrostatic cloud model used for the simulations. SAM solves the quasi-anelastic (Chorin 1967; Anderson et al. 1985) Navier–Stokes equations for the following: three-dimensional Cartesian wind components, pressure, potential temperature, mixing ratios of water vapor (qv), cloud water (qw), and rain (qr), and subgrid turbulent kinetic energy (Carpenter et al. 1998). SAM works with a number of ice microphysics packages including 3-ICE and a similar LFO83-like package with 10 ice classes (Straka and Mansell 2004, manuscript submitted to *J. Appl. Meteor.*, hereafter SM04). The lateral boundaries of the model domain are open. The upper and lower boundaries are free slip with $w = 0$ there. A Rayleigh damper is applied above 17 km to damp spurious gravity waves in the stratosphere. A constant vertical grid spacing of 500 m is used. The horizontal grid spacing is 1 km. As in Weisman and Klemp (1984), the domain is translated at constant velocity (see Table 1 of GSR2004). This allowed the storm updrafts to remain within the 90 km × 90 km × 20 km domain over the 2 h of simulation. A larger domain would be required to prevent anvil-

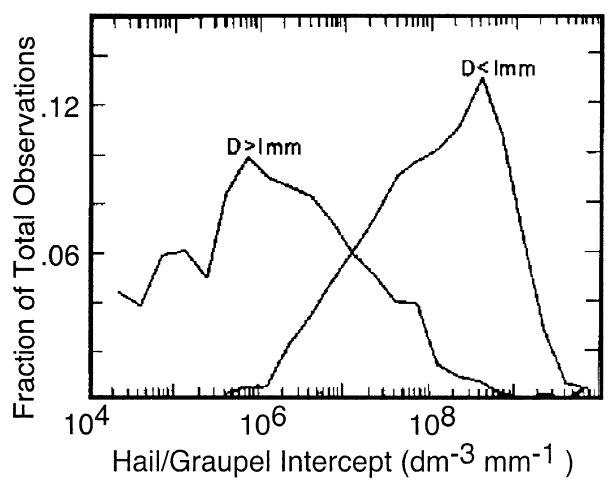

FIG. 1. Relative frequency of the slope intercept parameter computed from hail and graupel particle distributions observed during the National Hail Research Experiment. The ''$D > 1$ mm'' and ''$D < 1$ mm'' curves refer to relative frequency distributions for different groups of particles. A hail spectrometer and foil impressions were used to define the distributions. Variations in slope intercept parameter were found within a single storm and between storms. [Adapted from Knight et al. (1982).]

TABLE 3. Guide to simulation naming convention for the main experiments. The simulations are named according to the treatment applied to the hail/graupel category. The treatments are labeled as N$a\rho b$, where a is the exponent in the intercept parameter, 4×10^{a} m^{-4}, and b is the first digit in particle density, b00 kg m^{-3}. Bulk particle densities for rain (1000 kg m^{-3}) and snow (100 kg m^{-3}) are kept constant for the main experiments. Intercept parameters for rain and snow are also kept constant at 8×10^{6} and 3×10^{6} m^{-4}, respectively, for the main experiments.

Case name	n_{oh} (m^{-4})	ρ_h (kg m^{-3})	Color key
Warm rain	N/a	N/a	Black
N2ρ9	4×10^{2}	900	Brown
N3ρ9	4×10^{3}	900	Red
N4ρ9	4×10^{4}	900	Orange
N5ρ9	4×10^{5}	900	Yellow
N4ρ4	4×10^{4}	400	Green
N5ρ4	4×10^{5}	400	Light blue
N6ρ4	4×10^{6}	400	Dark blue
N7ρ4	4×10^{7}	400	Violet
N8ρ4	4×10^{8}	400	Pink

level precipitation from leaving the lateral domain boundaries starting at about $t = 90$ min. Model output was dumped at 3-min intervals for postanalysis.

b. Initial conditions

The model was run with an idealized temperature and moisture profile described by Weisman and Klemp (1984, hereafter WK84). This sounding has a CAPE of 2200 J kg^{-1}. Three of the idealized half-circle hodographs from WK84 were tested; these have arc lengths of Us = 20, 30, and 50 m s^{-1} (mean wind shear of 4×10^{-3}, 6×10^{-3}, and 10×10^{-3} s^{-1}, respectively) over the lowest 5 km. Above 5 km, the u and v wind–wind components are held constant. With this sounding, the 30 and 50 m s^{-1} profiles are known to support long-lived supercell storms, while the 20 m s^{-1} wind profile supports multicells (e.g., WK84; GSR2004).

Storms were initiated with a spheroid-shaped thermal having maximum perturbation of 1°C in its center at 1.4 km AGL (WK84) and varying as the cosine squared to the 0°C perturbation at its edge (Klemp and Wilhelmson 1978). The thermal has a horizontal radius of 10 km and a vertical radius of 1.4 km (WK84).

c. Microphysics treatments

The following treatments were applied. For the main experiments, the n_{oh} and ρ_h constants for the qh category were varied one at a time while all other microphysics parameters were kept constant (such as those describing the rain and snow distributions) for both Us = 30 and 50 m s^{-1} shear profiles. Distributions were chosen that span the range of observed intercept and particle densities discussed in section 2 (Table 3; Figs. 2a and 2b). The treatments are labeled as N$a\rho b$, where a is the exponent in the intercept parameter, 4×10^{a} m^{-4}, and b is the first digit in particle density, b00 kg m^{-3}. Each qh distribution intersects the y axis at the value of the intercept parameter (Fig. 2a). The treatments range from qh distributions where the mass is weighted heavily toward small graupel to distributions weighted heavily toward large hail (Fig. 2b). Because of this, the N8ρ4 and N3ρ9 cases are hereafter referred to as the ''small graupel'' and ''large hail'' cases, respectively. The N2ρ9 case (at Us = 50 m s^{-1}) was additionally performed at the request of an anonymous reviewer to acknowledge that many of the earlier hailstorm observations (Table 2; Fig. 1) may not have included a supercell with extremely large hail.

After the Us = 30 and 50 m s^{-1} cases established

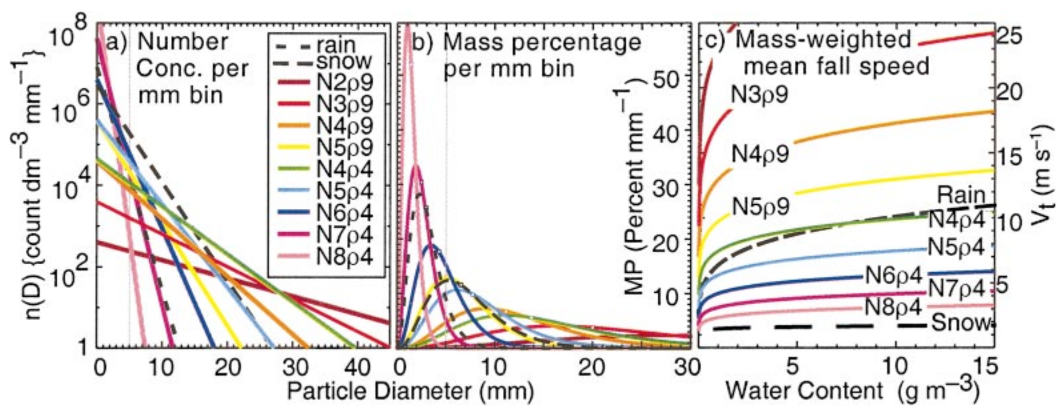

FIG. 2. (a) Number concentration per mm diameter size and (b) mass percentage per mm diameter size for a total water content of 10 g m^{-3} for rain, snow, and hail/graupel species. The overlaid dot in (b) corresponds to the diameter of the median mass of the distribution. (c) Mass-weighted mean terminal fall speed vs water content for the three species at $z = 4.5$ km ($\rho_{air} = 0.76$ kg m^{-3}). Line styles are given in the key. The faint vertical gray line shows the 5-mm diameter delineation between graupel and hail. The treatments applied to the hail/graupel category are labeled as N$a\rho$b, where a is the exponent in the slope intercept parameter, 4 × 10a m^{-4}, and b is the first digit in particle density, b00 kg m^{-3}.

the precipitation sensitivity, the N3ρ9 and N8ρ4 cases were tested for Us = 20 m s^{-1} to see whether the results were valid for groups of multicell storms as well.

Both a smaller particle density and a larger intercept parameter act to decrease the fall velocity over all ranges of water content (Fig. 2c). The N8ρ4 (small graupel) case, therefore, has the slowest qh fall speeds while the N2ρ9 case has the fastest.

4. Results and discussion

It was our intention to investigate the influence of the microphysics on the entire storm system—not just the right-moving supercell. Thus, unless otherwise indicated, all of the storms in the domain are analyzed simultaneously when computing the various statistics shown below. All runs were analyzed using history files archived at 3-min intervals.

Overview of the differences for the main experiments

It will be shown that when the qh distribution is weighted toward small graupel, faster qh production results and is associated with greater latent heating, slightly faster updrafts, and more widespread condensate. Because of slower fall speeds, qh leaves the storm at a higher level with smaller qh mass and is slower to precipitate to ground. Much less rain and no severe hail reaches ground in those cases.

1) UPDRAFT

Individual updraft maxima (Fig. 3) and the time series of domain updraft maximum (Fig. 4) are slightly larger for the small-graupel case than the large-hail case (for both Us = 30 and 50 m s^{-1}). This is corroborated in the small-graupel case where the southernmost supercell updraft (Us = 50 m s^{-1}) is continually larger in cross-sectional area than the large-hail case after 30 min (Figs. 3g and 31; Table 4). Cross-sectional areas and updraft maxima for the other cases (shown in Figs. 3 and 4; Table 4) vary between the large-hail and small-graupel cases. The cases with qh distributions weighted toward smaller graupel also tend to have larger total updraft volumes for all storms integrated over the domain (snapshots in Table 5).

Cases supporting stronger updrafts are associated with greater time-averaged maximum temperature perturbations (Figs. 5a and 5b). To understand why the latent heating is apparently larger in the small-graupel case (N8ρ4), hypothetical rates were first plotted for N3ρ9 and N8ρ4 using assumed mixing ratios. All of the following qh production and loss rates influenced by ρ_h or n_{oh} increased in magnitude between N3r9 and N8r4: qhaci, qhacr, qhacs, qhacw, qhdpv, qvsbh, and qrmlh (see rate key in the appendix). A diagnostic plot of these equations using assumed mixing ratios can be found in Fig. 6 of Gilmore et al. (2002).

Because such an analysis only gives a guess as to the expected behavior, actual model mass transfer rates are evaluated at t = 30, 60, 90, and 120 min. Two times (t = 30 and 90 min) are shown in Figs. 6 and 7. One can see that the fusion and deposition heating associated with qh growth (qhacw, qhacr, and qhdpv) are indeed much larger as one moves toward the small-graupel regime (Figs. 6c and 7c). Most important, the domain heating from the net condensation rate is much larger toward the small-graupel regime (qwcdv − qvevw; Figs. 6d and 7d) and as such could not be predicted from a simple analysis of the model equation sets. Also, the changes in heating contributions from fusion and deposition growth of snow and cloud ice are negligible in comparison (Figs. 6e, 6f, 7e, and 7f). The rates presented in Figs. 6 and 7 are visited again in the next section.

One caution should be mentioned regarding Figs. 6 and 7: domain-total rates are a function of both the amount of mixing ratio available at each grid box as well as the volumetric coverage. Large volumes of small rates might have the same domain total as small volumes of large rates. Thus, the domain-total rates must be interpreted alongside the other evidence presented herein.

2) PRECIPITATION STRUCTURE

The time-averaged horizontally summed qh mass (Figs. 8a and 8e) and the time-averaged maximum temperature perturbation (Figs. 5a and 5b) are maximized at a higher altitude as one moves from the large-hail (N3ρ9) case to the small-graupel (N8ρ4) case. Not only is qh domain-total growth enhanced (Figs. 6 and 7) and total precipitation volume enhanced (Table 6), but qh is lofted to higher altitudes as one moves toward the small-graupel (N8ρ4) case. Because the terminal fall speed is reduced, upward qh fluxes within the updraft are enhanced (not shown), and qh must spend less time in the updraft, resulting in smaller maximum values of qh (Table 7). The greater upward fluxes result in higher-altitude transport of qh (Figs. 8a and 8e). After leaving the updraft, the smaller terminal fall speed results in a longer qh residence time aloft, and qh is more susceptible to horizontal advection by the environmental winds. More expansive precipitation volumes (Table 6) result and explain why the horizontally summed qh values are larger as one moves from N3ρ9 to N8ρ4 (Figs. 8a and 8e) despite the maximum qh values showing the opposite trend (Table 7).

For instance, at t = 90 min and Us = 50 m s^{-1}, the small-graupel case (N8ρ4) has the largest volumes of total precipitation mixing ratio (greater than 0.1 or 2.1 g m^{-3}; Table 6). In contrast, only the hail-weighted regime has large volumes of large total precipitation (greater than 8.1 or 10.1 g m^{-3}; Table 6). These comparisons are also valid for Us = 30 m s^{-1} (not shown) and t = 30, 60, and 120 min. The other cases shown vary between the large-hail (N3ρ9) and small-graupel (N8ρ4) cases. Consistent with this, east–west vertical

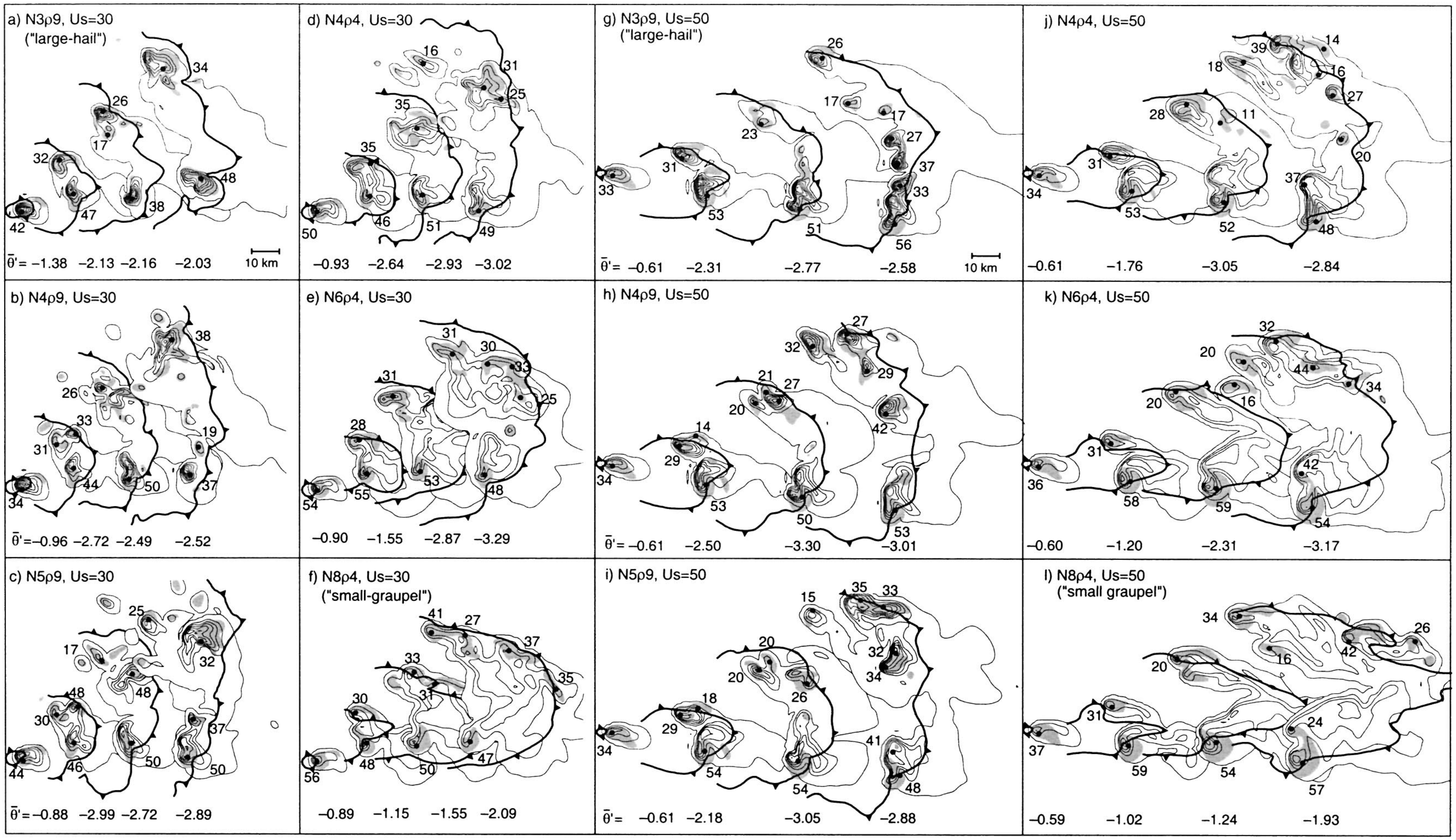

FIG. 3. Evolution in midlevel storm structure depicted at 30, 60, 90, and 120 min for (a)–(f) Us = 30 m s^{-1} and (g)–(l) Us = 50 m s^{-1}, for six variations in the three-class ice microphysical scheme. Total precipitation mixing ratio at z = 4.75 km is contoured at 2 g kg^{-1} intervals beginning at 0.1 g kg^{-1}. Regions of updraft > 5 m s^{-1} at z = 4.75 km are shaded with the updraft maxima (anywhere in the vertical) located by dots and labeled in m s^{-1}. The leading edge of the surface gust front (−0.5°C perturbation potential temperature isotherm) is denoted by a thick barbed line. The minimum area-averaged perturbation potential temperature (enclosed by the −0.5°C isotherm) for each time is also shown at the bottom of each panel for each time. The N2ρ9, N5ρ4, and N7ρ4 plots are omitted for the sake of brevity. See GSR2004 for the warm-rain case.

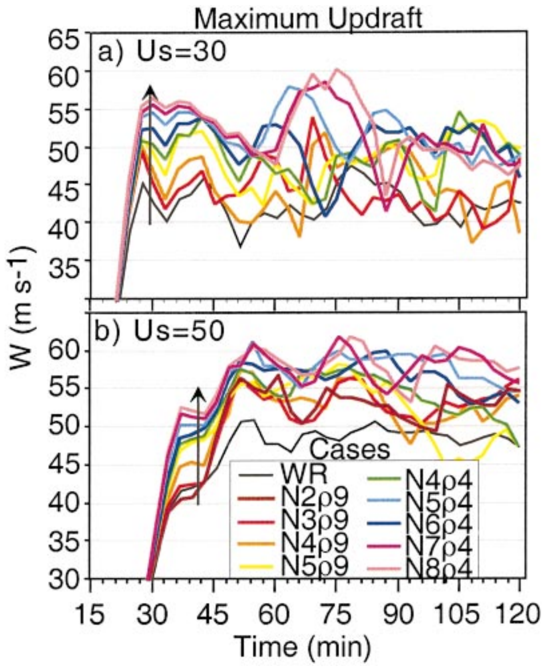

FIG. 4. Maximum updraft in the domain as a function of time for (a) Us = 30 m s^{-1} and (b) Us = 50 m s^{-1}. See key for line-style coding. Arrows show the general direction of change from the large-hail case (N3ρ9) to the small-graupel case (N8ρ4). The warm-rain (WR) case from GSR2004 is also included for reference, and the N2r9 case is included for Us = 50 m s^{-1}.

cross sections through the strongest storm updraft at t = 60, 90, and 120 min reveal a greater portion of qh within the anvil region marching toward the N8ρ4 case (not shown). This is similar to the sensitivity reported by McCumber et al. (1991).

Total (and maximimum values of) qs and qi become more scarce moving from the large-hail (N3ρ9) to small-graupel (N8ρ4) cases (Figs. 8b, 8c, 8f, and 8g; Table 7). This is due primarily to reduced qs and qi production rates toward small graupel (Figs. 6e, 6f, 7e, and 7f) rather than increased scavenging by qh. Also note that the amount of qw decreases (increases) above (below) z = 5 km toward the small-graupel case. This is apparently associated with the shifting of qh toward higher altitudes (Fig. 8).

Total precipitation mass fallout and rain depths integrated over 2 h are maximized for the N4ρ9 case (Fig. 9; Table 8).[2] This is consistent with the rates that show a net maximum rain production near N4ρ9 (Figs. 6a and 7a; also true at t = 60 and 120 min; not shown). A greater fraction falls as qh for the N3ρ9 and N2ρ9 cases (Table 8), with slightly less total mass reaching the ground. In contrast, going toward small graupel, less qh and qr mass accumulates at the ground. In fact, the total mass fallout is about 4(3) times less for N8ρ4 compared to N3ρ9 for Us = 50 m s^{-1} (Us = 30 m s^{-1}). The ratio drops to about 2 times less for a nonsupercell regime of Us = 20 m s^{-1}. Thus, accumulated precipitation differences decrease with decreasing shear.

Additionally, in cases with less precipitation reaching ground over time, more precipitation remains aloft (Fig. 10) because of the slower fall speed (Fig. 2c). That qh that does reach the melting level is spread over a larger area (not shown; similar to Table 6) and with smaller amounts at each grid box (Table 7), results in smaller qr amounts after melting (Table 7). Complete melting occurs at a higher altitude (inferred from Figs. 8a and 8e), and therefore qr has more time to evaporate before reaching ground marching toward the small-graupel case.

Moreover, greater crop damage can be inferred from the N2ρ9 or N3ρ9 cases than the N8ρ4 case because of

[2] As explained in GSR2004, the accumulated rainfall and hailfall estimates were computed by diagnosing the rain and hail precipitation rates for the lowest model grid level at 3-min intervals and then assuming constant fluxes for each 3-min period. A Richardson's extrapolation analysis reveals that this technique underestimates the total precipitation accumulation by about 4% for the N4ρ9 case. Once hail and rain has fallen to the ground, it retains its phase and no longer interacts with the model.

TABLE 4. Cross-sectional (XY) area of the southernmost supercell main updraft (greater than 5 m s^{-1}) at z = 4.75 km and four simulation times. The case with the maximum area at a particular time is highlighted in boldface type. The warm-rain case is included for reference.

	Updraft area (km^2) at			
Us = 50 m s^{-1} case	t = 30 min	t = 60 min	t = 90 min	t = 120 min
Warm rain	44	50	85	98
N2ρ9	47	57	69	85
N3ρ9	50	60	69	76
N4ρ9	50	60	72	66
N5ρ9	50	57	69	63
N4ρ4	47	57	82	91
N5ρ4	50	60	88	98
N6ρ4	50	66	**107**	123
N7ρ4	50	66	**107**	126
N8ρ4	50	**69**	**107**	**139**

TABLE 5. Updraft volume greater than 10 m s^{-1} integrated below the anvil level ($z \leq 9$ km) over the domain at four simulation times. The case with the maximum (minimum) area at a particular time is highlighted in boldface (underlined) type. The warm-rain case is included for reference.

	Domain updraft volume (km^3) at			
Us = 50 m s^{-1} case	t = 30 min	t = 60 min	t = 90 min	t = 120 min
Warm rain	<u>148.0</u>	<u>420.0</u>	<u>614.5</u>	<u>915.0</u>
N2ρ9	187.5	483.5	787.0	1003.0
N3ρ9	189.5	497.5	624.5	1124.5
N4ρ9	192.0	516.0	690.5	1291.5
N5ρ9	194.5	524.0	694.0	1344.0
N4ρ4	187.0	513.5	669.5	1158.0
N5ρ4	185.5	540.5	838.5	1207.5
N6ρ4	194.5	554.5	867.0	1352.0
N7ρ4	196.5	**558.0**	846.5	1491.5
N8ρ4	**196.5**	549.5	**950.5**	**1694.0**

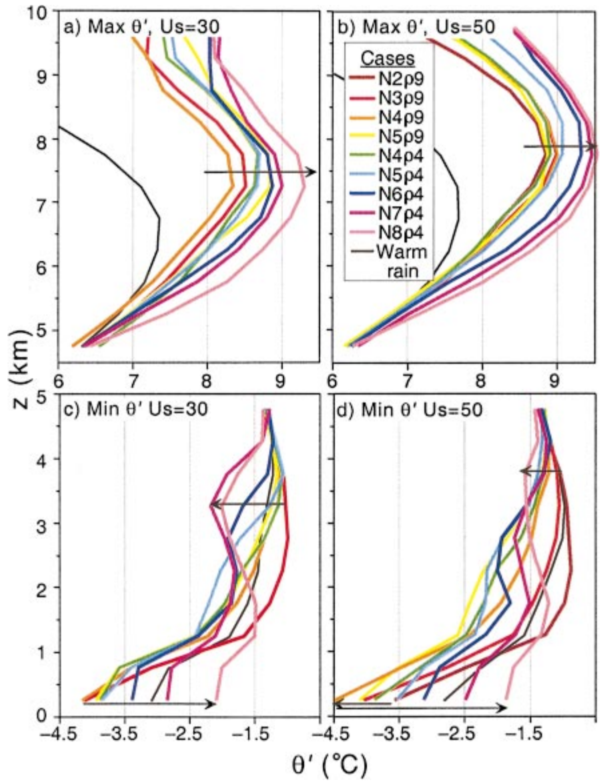

FIG. 5. Time-averaged height profiles of (a) maximum θ' and (c) minimum θ' for Us = 30 m s^{-1} for the eight variations in the ice microphysical parameterization. (b), (d) As in (a), (c), respectively, but for Us = 50 m s^{-1} cases (including the additional N2ρ9 case). The average was computed using model data sampled every 3 min from t = 3 to t = 120 min. See the key in Fig. 4 for line styles. Arrows show the general direction of change from the large-hail case (N3ρ9) to the small-graupel case (N8ρ4). The warm-rain case from GSR2004 is also included for reference.

locally larger accumulated qh mass there (Fig. 9). Although hailstone crop damage also varies according to crop characteristics and near-ground wind conditions, accumulated hail mass is a primary factor (Changnon 1971, 1999).

Moreover, property damage is a function of the maximum hail sizes produced by a storm (e.g., Changnon 1999). One way to assess the property damage potential is to convert the continuous size distribution of hailstones fallen to the ground for each case into a discrete size distribution. First, counts of accumulated hail/graupel are determined for 0.01-mm size bins. These counts are then used to integrate the mass over particular size ranges. The mass for each range can then be redistributed into a single representative size to obtain a count. In our analysis, counts were computed for representative diameters of the following sizes: graupel (2.5 mm), pea (6 mm), marble (12.5 mm), quarter (25.5 mm), golf ball (44 mm), baseball (70 mm), and softball (114 mm). The total count for each representative size at the location of maximum qh mass accumulation is shown in Table 9. The largest hailstones fall to the ground in the N2ρ9 case while three of the cases produce only graupel (N6ρ4, N7ρ4, and N8ρ4; Table 9).

For the large-hail case (N3ρ9) at Us = 50 m s^{-1}, over 4900 golf-ball-sized hailstones (and 45 baseball-sized stones) per 100 m^2 footprint fell to the ground over 2 h (Table 9) at the maximum qh accumulation location ($\times$ symbol in Fig. 9a). A 100 m $\times$ 100 m footprint covers roughly the ground-projected area of a roof for a small-sized home. Only a single golf-ball-sized hailstone will cause damage to six of nine types of common roofing materials over 90% of the time, and a single baseball-sized stone will damage all common roofing materials (Marshall et al. 2002). Thus, roof devastation can be inferred for the maximum hailfall location in the N2ρ9 and N3ρ9 cases. (Also, owing to the presence of baseball- and softball-sized hailstones, greater potential injury to livestock and persons can be inferred for those cases.) In contrast, lesser roof damage would be expected for N4ρ9, and little to no roof damage would be expected for all other cases. Because only graupel reaches the ground for N6ρ4, N7ρ4, and N8ρ4, no hail-induced roof or crop damage would be expected there. For the Us = 30 m s^{-1} cases, roof damage would still be expected for N3r9, with 39 baseball-sized stones per 100 m^2 (not shown). However, the inferred property damage for each case would be less because of fewer hailstones in each category (not shown).

It is important to realize that the greatest hailstone accumulations are not always associated with the right-moving supercell. Five of the 12 cases shown in Fig. 9 have the maximum qh accumulations associated with the less organized multicell convection to the north. Thus, these results are relevant for the entire storm system.

In summary, marching toward N8ρ4, one finds that qh is produced faster (Figs. 6c and 7c); however, the qh water contents produced (at individual grid boxes) are smaller (Table 7; Figs. 10c and 10d) and are spread over a larger volume (Table 6). This is due to the smaller parameterized qh fall velocity (Fig. 2c), which results in lofting of qh to a higher altitude (Figs. 8a and 8e), slower downward qh fluxes (not shown), and, consequently, longer residence times aloft. This results in less ground accumulations of precipitation (Table 8; Figs. 9f, 9l, 10a, and 10b). Furthermore, the amount of hail damage inferred from each case is directly related to the choice of how qh is parameterized with devastating hail damage in N2ρ9 and no hail damage for N6ρ4, N7ρ4, and N8ρ4.

3) MIDLEVEL COOLING, DOWNDRAFTS, AND COLD POOLS

The time-averaged minimum temperature profiles (Figs. 5c and 5d) reveal that, near the environmental melting level (between z = 2.25 and 3.25 km), the temperature is lower and more pronounced for those cases with larger intercepts (smaller graupel). Also, the cool-

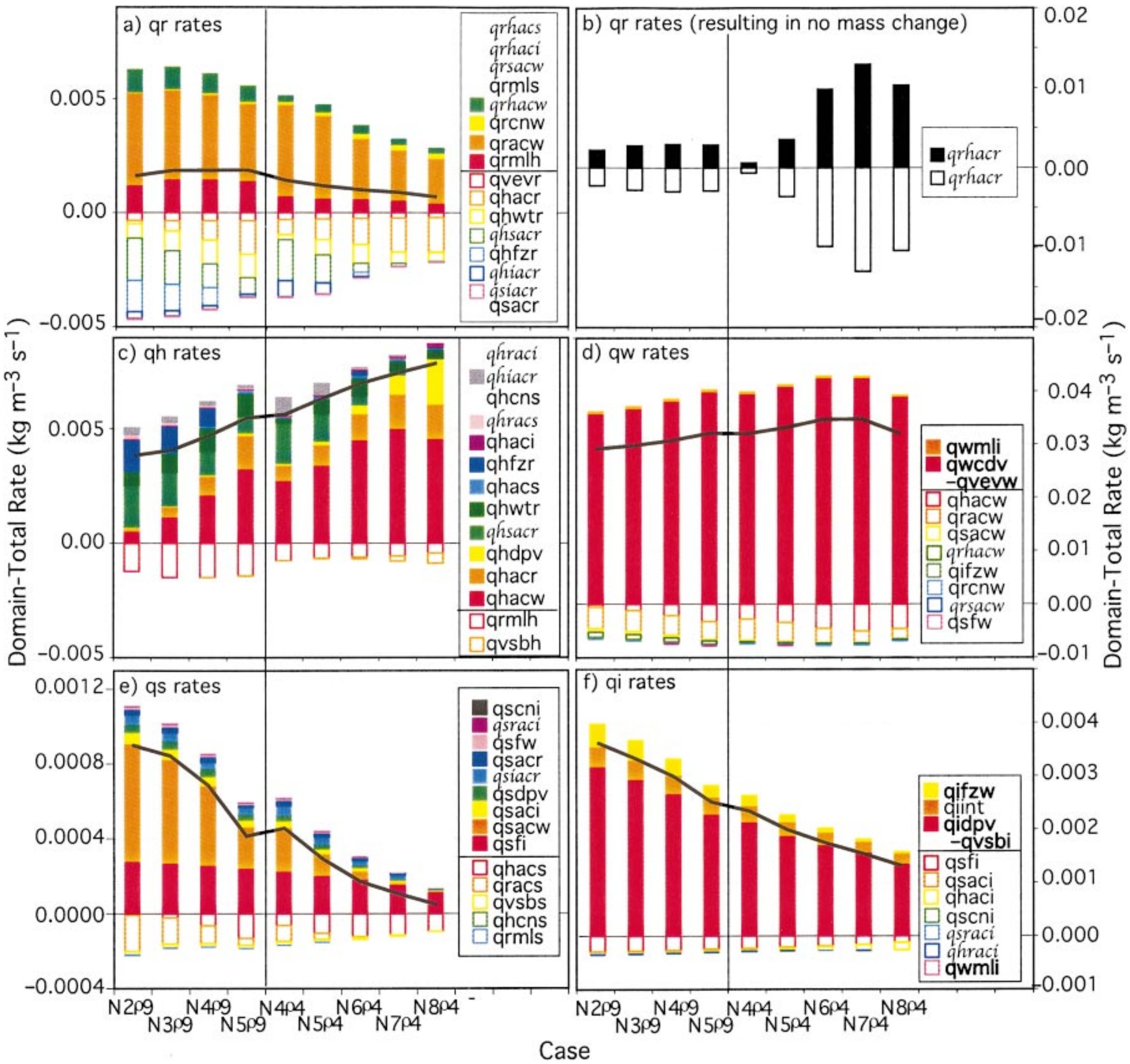

FIG. 6. Total production and loss rates summed over the domain for each of the Us = 50 m s^{-1} cases at t = 30 min for (a) qr, (b) qr resulting in no mass change, (c) qh, (d) qw, (e) qs, and (f) qi. The rates are stacked using the order of importance from t = 90 min (see Fig. 7) with a rainbow color pallet ranging from the largest bars (red) to smallest bars (violet). Gains (losses) are represented by filled (unfilled) bars. The net rate is represented by a solid black line. Three-body interactions are indicated in script, and saturation adjustment processes are indicated in bold. The species experiencing the gain (loss) is represented by the second (last) letter. Additionally, three-body interactions include an extra letter (third position) in the name for the accreting species when it differs from the gain species. A vertical line separates the ρ_h = 900 kg m^{-3} cases from the ρ_h = 400 kg m^{-3} cases.

ing begins at a higher altitude (Figs. 5c and 5d) for the smaller-graupel cases that have slower qh terminal fall velocity (Fig. 2c). However, the minimum temperature differences between cases are largest near ground. Case N4ρ9, which also has the most low-level rainfall, has the coldest time-averaged minimum temperatures within the outflow (Figs. 5c and 5d). The minimum time-averaged temperatures at the ground *warm* both toward the large-hail and small-graupel regimes. Consistent with these minimum temperature profiles, the coldest low-level outflow is associated with the strongest downdrafts near ground (z = 500 m; Fig. 11).

However, the time-averaged minimum temperature profiles cannot show important temporal variations. The coldest area-averaged (not minimum) low-level outflow temperature occurs at later times marching toward the small-graupel regime (bottom of Fig. 3 panels). For example, at t = 30, 60, 90, and 120 min, the coolest (horizontally averaged) low-level outflow is found in N3ρ9, N4ρ9, N4ρ9, and N6ρ4, respectively (Fig. 3; Us = 50). Similar behavior occurs for Us = 30 m s^{-1}. Thus, the coldest area-averaged outflow for all simulations occurs later, marching toward smaller graupel. One wonders whether the N8ρ4 case might eventually

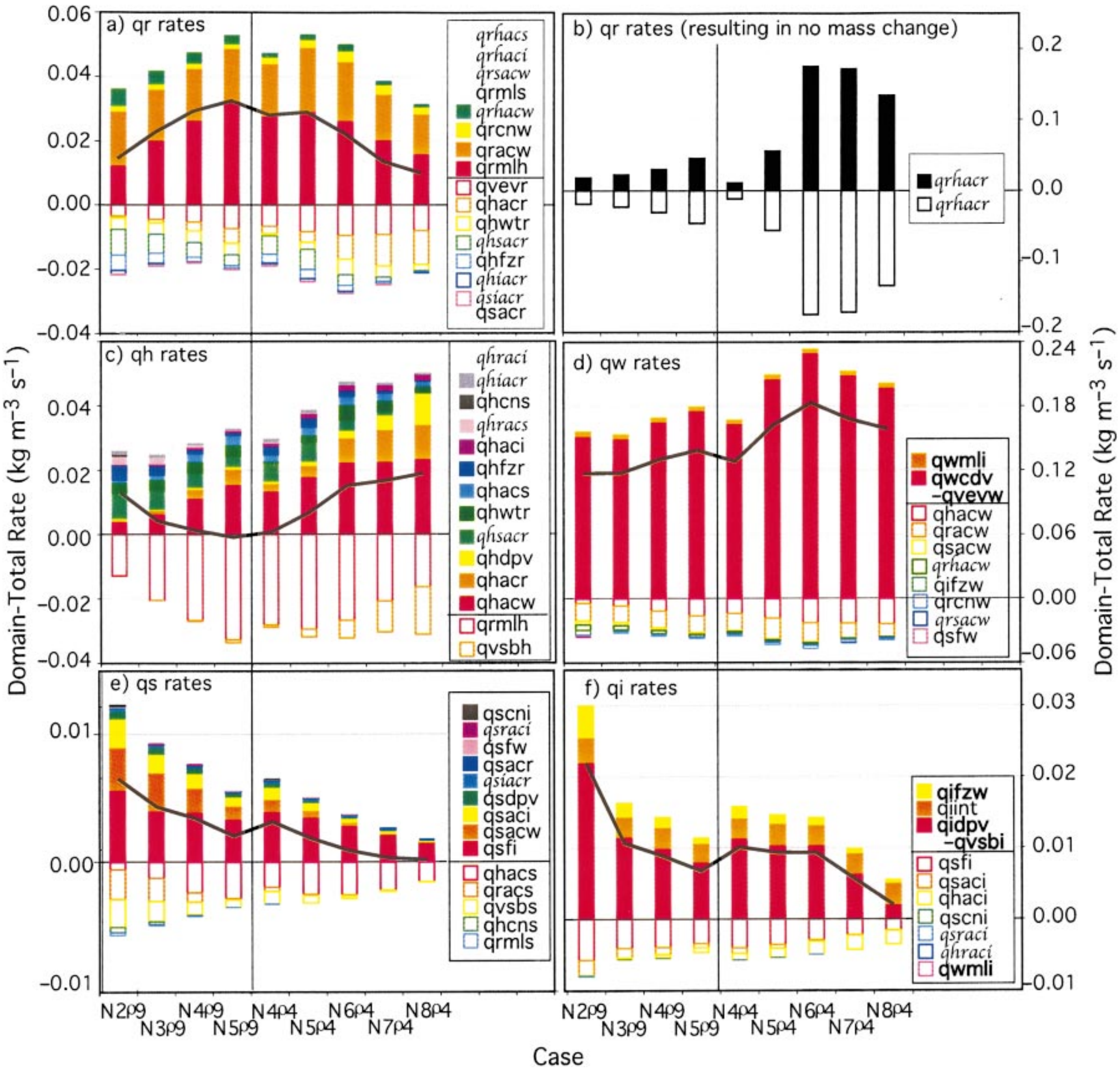

FIG. 7. Same as Fig. 6, except for $t = 90$ min. The processes in (a)–(f) have the same colors as in Fig. 6 to ease comparison.

provide the coldest outflow if the simulations continued past $t = 2$ h.

The temperature of the downdraft and cold pool is a function of both the available qh as well as the qh distribution characteristics. Assuming the same qh amount, loss rates must increase as one marches toward the small-graupel regime (not shown). However, the cases weighted toward smaller graupel have smaller qh at each grid point (Table 7) but for larger volumes (Table 6) and occurring at a higher altitude (Figs. 8a and 8e). Therefore, domain-total melting, sublimation, and subsequent evaporation rates (Figs. 6 and 7) and associated cooling are spread over a larger area and begin at a higher altitude in the small-graupel regime. The qh almost completely melts by about $z = 2$ km in the graupel-weighted regime. (Figs. 8a and 8e), and it melts to create smaller qr amounts per grid box (not shown). Those smaller qr amounts then evaporate more easily before reaching the ground. In contrast, cooling is apparently limited in N2ρ9 because not enough qh melts (Fig. 7c). This is due to both the large parameterized fall speeds (Fig. 2c) and the slower parameterized melting rates dictated by the large-hail regime.

The accumulated rainfall beneath the simulated storms was much less sensitive to order-of-magnitude increases/decreases in the snow intercept and rain intercept (experiments not shown). We agree with an anonymous reviewer who suggested this is primarily because order-of-magnitude changes in rain or snow intercept parameters correspond to smaller terminal velocity changes than those for qh. Observed rain and snow intercept parameters vary by at least two orders

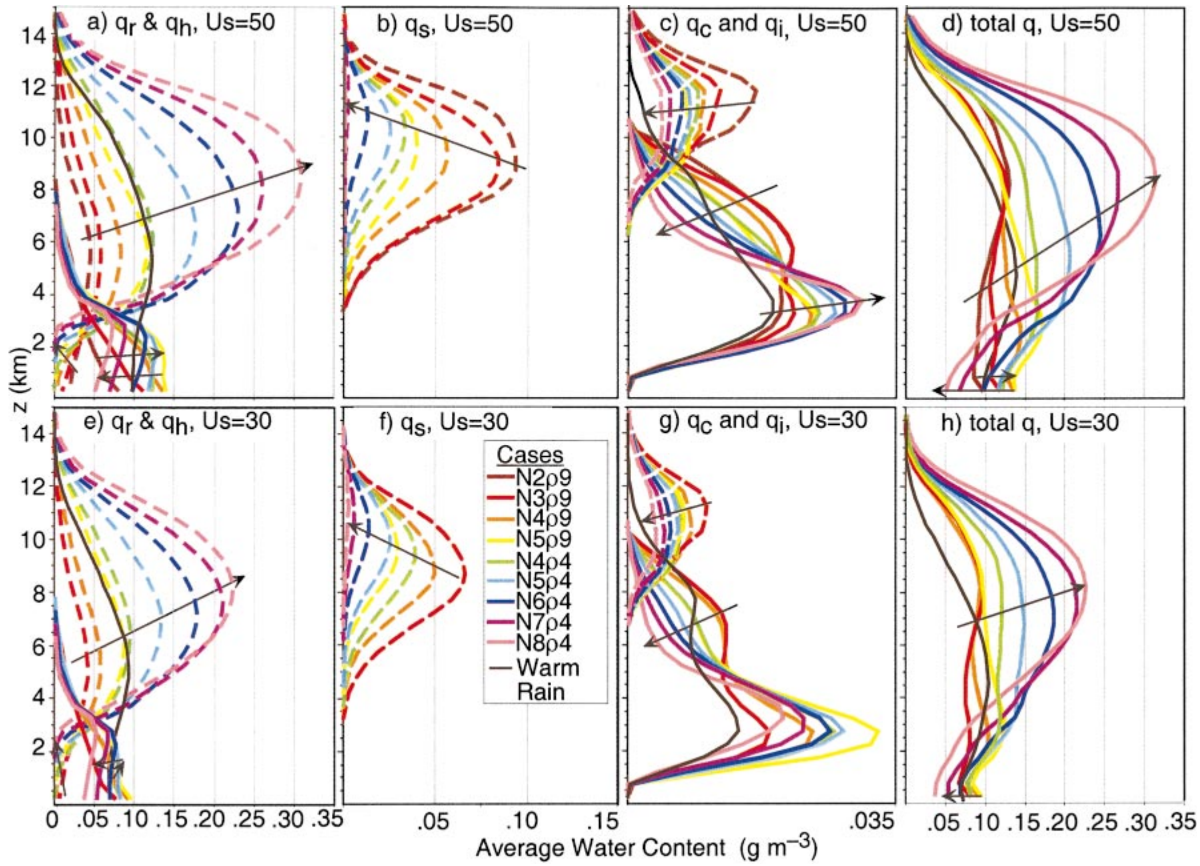

FIG. 8. Temporally and spatially averaged water content (g m^{-3}) as a function of height over the entire domain for the 19 cases in the study. The following species are shown for Us = 50 m s^{-1} cases: (a) rain and hail/graupel, (b) snow, (c) cloud water and cloud ice, and (d) total water. (e)–(h) Same as (a)–(d), except for Us = 30 m s^{-1} cases. (N2ρ9 is included only for Us = 50 m s^{-1}.) Dashed lines in (a)–(c) and (e)–(g) represent the ice phase, while solid lines represent the liquid phase. Temporal averaging was performed upon data output with 3-min frequency from t = 3 to 120 min. Spatial averaging was performed horizontally with every point in the 90 km × 90 km grid. Arrows in (a)–(d) show the general direction of change from the large-hail case (N3ρ9) to the small-graupel case (N8ρ4). The warm-rain case is also included for reference.

of magnitude (e.g., Marécal et al. 1993; Ulbrich 1983; Houze et al. 1979; Heymsfield et al. 2002a). Future studies should investigate the interactions that may result when several intercept parameters for different species are varied simultaneously.

TABLE 6. Domain-total volume (km^3) of total precipitation content at t = 90. "Total" precipitation content at each grid cell is defined as the sum of the rain, snow, and hail/graupel contents. The simulation possessing the largest volume for a particular content is highlighted in boldface type. The warm-rain case is included for reference.

Us = 50 m s^{-1} case	Volume (km^3) of precipitation content (g m^{-3}) greater than					
	0.1	2.1	4.1	6.1	8.1	10.1
Warm rain	11 358.0	2865.0	1326.5	249.0	—	—
N2ρ9	22 720.0	1083.0	551.0	266.0	**115.0**	37.0
N3ρ9	21 502.0	1463.5	654.0	279.5	113.0	**39.5**
N4ρ9	22 027.5	2209.5	917.5	**300.0**	64.5	9.0
N5ρ9	21 690.0	3048.0	**1143.0**	234.0	3.0	—
N4ρ4	24 012.5	3650.5	1033.0	102.0	—	—
N5ρ4	24 319.0	5017.0	987.0	22.5	—	—
N6ρ4	24 146.5	5653.5	1094.0	10.0	—	—
N7ρ4	24 038.5	5873.5	909.0	16.5	—	—
N8ρ4	**25 404.0**	**6424.0**	694.0	6.0	—	—

TABLE 7. Maximum value of perturbation water contents anywhere in the domain over the 2-h simulation. Bold (underlined) text represents the largest (smallest) values.

Us = 50 m s^{-1} case	Maximum water content (g m^{-3}) of					
	qv	qw	qr	qi	qs	qh
Warm rain	3.11	3.36	8.77	N/a	N/a	N/a
N2ρ9	3.09	3.35	9.51	**1.44**	**1.66**	12.53
N3ρ9	3.12	3.35	11.47	1.14	1.53	**13.44**
N4ρ9	3.09	3.39	**11.81**	0.95	1.04	10.81
N5ρ9	3.08	3.45	10.83	0.69	0.58	9.42
N4ρ4	3.10	3.40	8.80	0.91	0.71	7.70
N5ρ4	3.13	3.44	8.67	0.75	0.42	6.99
N6ρ4	3.14	**3.45**	7.53	0.57	0.21	6.96
N7ρ4	**3.16**	3.40	7.02	0.44	0.12	6.19
N8ρ4	3.14	3.37	7.09	0.37	0.06	6.16

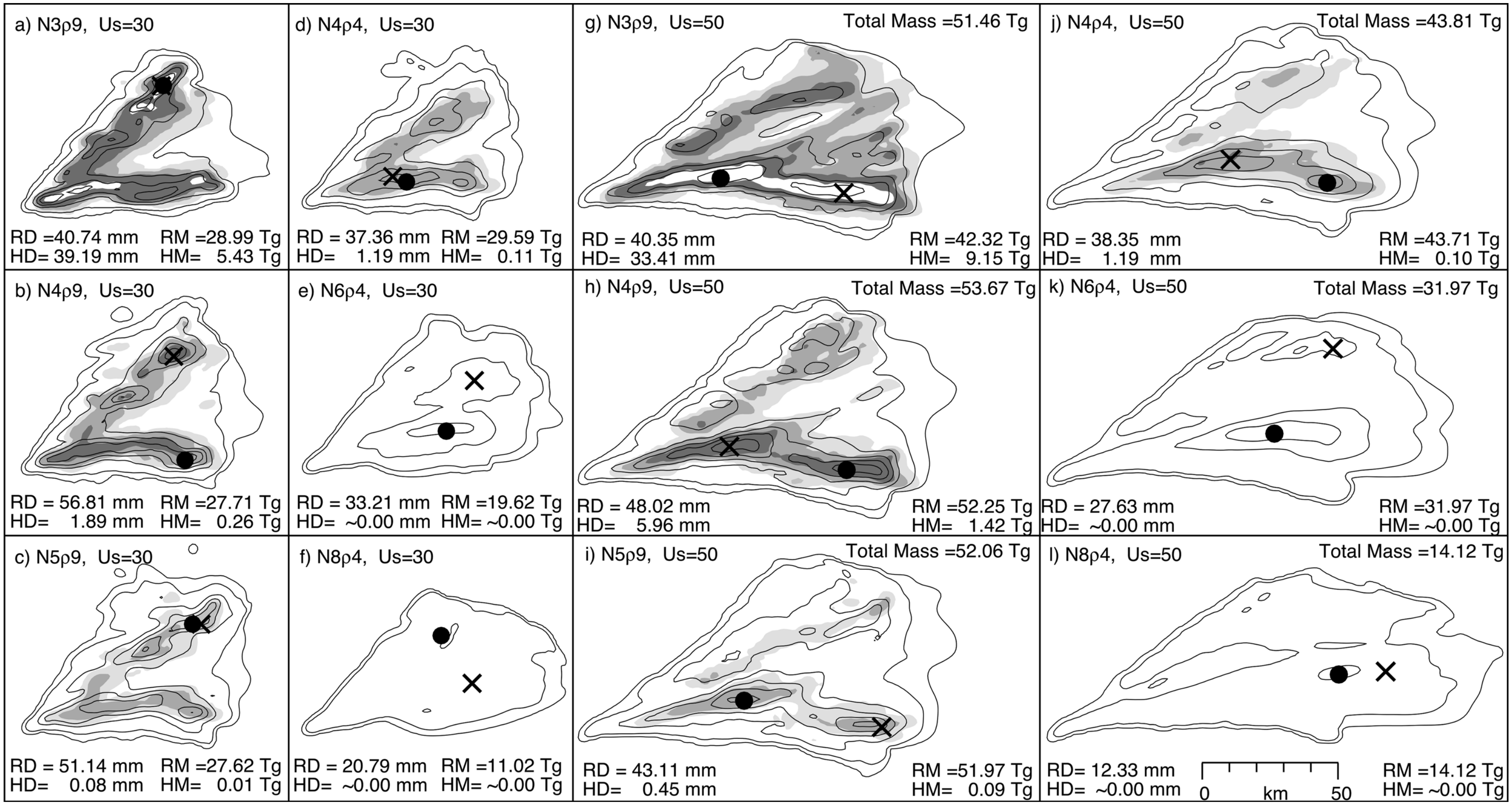

FIG. 9. Ground-accumulated rain and hail/graupel over 2 h for 12 of the cases. Cases are stratified by vertical wind shear and by microphysical parameterization as described in Table 3. (a)–(f) Us = 30 m s^{-1}, and (g)–(l) Us = 50 m s^{-1}. Rain contours (isohyets) shown are 0.1, 1, 10, 20, 30, 40, and 50 mm. Light gray, medium gray, dark gray, and white shading is shown for hail/graupel depths greater than 0.01, 0.1, 1, and 10 mm, respectively. RD refers to the maximum rain depth (mm) experienced over the area at a point, and RM refers to the total mass of rain fallen over the area (Tg). HD and HM have similar definitions for hail/graupel. The $\times$ (filled circle) in each figure marks the location of the maximum hail/graupel (rain) accumulation. The N2ρ9, N5ρ4, and N7ρ4 cases are omitted for the sake of brevity.

TABLE 8. Accumulated precipitation total (rain plus hail/graupel) mass and percentage of total mass that is hail/graupel at the surface for each of the main experiments.

	Accumulated mass on ground			
	Us = 30 m s^{-1}		Us = 50 m s^{-1}	
Cases	Total (Tg)*	Hail/graupel (% of total)	Total (Tg)	Hail/graupel (% of total)
Warm rain	26.01	N/a	36.40	N/a
N2ρ9	N/a	N/a	52.05	44.51
N3ρ9	34.42	15.77	51.46	17.78
N4ρ9	35.17	2.05	53.67	2.64
N5ρ9	35.41	0.31	52.06	0.17
N4ρ4	29.70	0.38	43.81	0.22
N5ρ4	28.43	0.01	40.10	0.007
N6ρ4	22.65	0.0002	31.97	0.0002
N7ρ4	16.80	<0.0001	20.60	<0.0001
N8ρ4	11.13	<0.0001	14.12	<0.0001

* Tg = teragrams (trillions of grams).

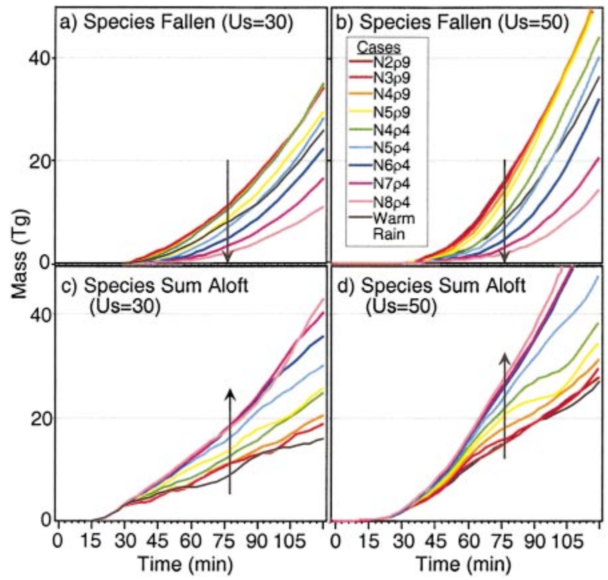

FIG. 10. Time series of (a), (b) cumulative precipitation mass fallen and (c), (d) cumulative precipitation mass aloft (Tg) for Us = 30 and Us = 50 m s^{-1} cases, respectively. (N2ρ9 is included only for Us = 50 m s^{-1}.) See key for the line styles representing each microphysical parameterization. Arrows show the general direction of change from the large-hail case (N3ρ9) to the small-graupel case (N8ρ4). The warm-rain case is also included for reference.

5. Discussion

The implications that these results have upon cloud-scale precipitation forecasting and the applicability of these results for other environments is now discussed. In addition, we comment on whether these results are relevant for understanding the differences between low- and high-precipitation-producing supercells. Differences between results found herein and found by other researchers are also discussed.

a. Forecast applications

Since the size distribution and density for each species vary widely among storms and even within a single storm, one main question arises for the forecaster. Which size distribution for each species (most importantly, for the qh species) should be used in a model? Could an ensemble of solutions prove useful to the precipitation forecaster?[3]

We suggest that the value of an ensemble of precipitation forecasts, similar to those shown herein, would be limited. This would hold true even if the ensemble members demonstrated a high level of skill in forecasting the storm type and evolutions. While one extreme (N3ρ9) might indicate the potential for localized

[3] Note that the researcher can ''tune'' the input parameters to obtain a model solution that best fits a particular case study. The forecaster does not have this luxury.

TABLE 9. Hail accumulation counts per 100 m^2 at the location of maximum hail/graupel mass accumulation for each of the experiments integrated over the 2 h of simulation for Us = 50 m s^{-1}. Counts of ''<1'' indicate less than 1 particle per 100 m^2 but at least 1 per km^2. Counts of ''—'' indicate less than 1 particle per 1 km^2.

Us = 50 m s^{-1} cases	Count of graupel and hail over a 100 m^2 area						
Integration range and representative diameter (mm)	0–5 Graupel (2.5)	5–7 Pea (6)	7–18 Marble (12.5)	18–33 Quarter (25.5)	33–55 Golfball (44)	55–85 Baseball (70)	85–143 Softball (114)
N2ρ9	3 989 175	546 548	1 063 116	259 931	43 381	3465	97
N3ρ9	14 175 962	1 565 448	1 615 386	134 805	4904	45	<1
N4ρ9	22 497 157	1 192 610	261 858	1112	<1	—	—
N5ρ9	5 293 028	10 742	119	<1	—	—	—
N4ρ4	6 350 524	261 505	36 368	38	<1	—	—
N5ρ4	361 283	29	<1	—	—	—	—
N6ρ4	15 555	—	—	—	—	—	—
N7ρ4	254	—	—	—	—	—	—
N8ρ4	141	—	—	—	—	—	—

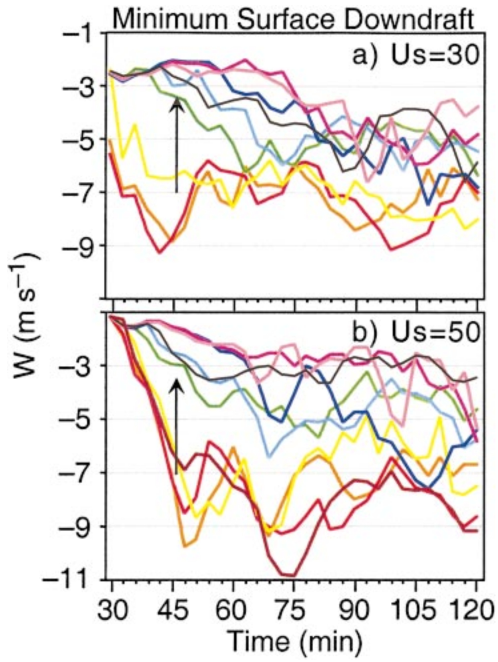

FIG. 11. Minimum ''surface'' ($z = 500$ m) downdraft in the domain as a function of time for (a) Us = 30 m s^{-1} and (b) Us = 50 m s^{-1}. See the key in Fig. 10 for line-style coding. Arrows show the general direction of change from the large-hail case (N3ρ9) to the small-graupel case (N8ρ4).

flash flooding and damaging hail, the other extreme (N8ρ9) would be innocuous by comparison.

Ferrier et al. (1995) have suggested that one can avoid the problem of picking an intercept a priori by predicting number concentration for an ice species in addition to its mixing ratio. Within the next several years, increasing computer power will allow the double-moment microphysics schemes of Ferrier (1994), RAMS (Meyers et al. 1997), and others to be efficient enough to run operationally on a regional basis. It is hoped that such schemes with less inherent uncertainty will give improved precipitation forecasts compared to the LFO83-like schemes. Perhaps single-moment schemes with more ice species would also give less inherent uncertainty (McCumber et al. 1991; SM04).

b. Implications for high- and low-precipitation supercells

The reader may wonder whether the large precipitation differences shown herein bear any resemblance to those observed in supercells that produce either visually low or high amounts of precipitation. These have been called low-precipitation (''LP'') or high-precipitation (''HP'') supercells (Moller et al. 1994). To a first-order approximation, LP supercells produce less ground-accumulated precipitation than HP supercells. In this sense, we are simulating the general behavior of LP and HP supercells. Additionally, the present simulation results suggest that some LP storms could in fact have very strong updrafts and simply suspend more water mass in slowly falling ice particles (such graupel or snow). This would contrast with earlier simulations suggesting that LP supercells may simply have weaker updrafts that produce less water mass (Brooks and Wilhelmson 1992).

However, the microphysical limitations of prescribing a constant intercept and density limit how well our LP simulations compare to the observations. For instance, hail distributions vary in density and intercept (e.g., Pruppacher and Klett 1978; Knight et al. 1982) depending upon their location in a hailstorm, and even nonsupercell thunderstorms vary in snow density and intercept throughout the anvil region (Heymsfield et al. 2002a,b). Also, observers of LP supercells frequently report baseball- or larger-sized hailstones and large raindrops despite a lack of heavy rain near the updraft (e.g., Moller et al. 1994). In contrast, our simulated LP supercell with small graupel (N8ρ4) had no hailfall (Tables 8 and 9) and rain particle size distributions similar to the HP (N3ρ9) case owing to the constant rain intercept. The lack of diversity in the qh and qr distributions is certainly limiting the extent to which the 3-ICE scheme or other LFO83-like schemes could hope to reproduce the observations.

c. Other qh-distribution-varying parameter studies for isolated storms

McCumber et al. (1991) were first to report on the influence that changes in the *qh* distribution could have on 3D numerical storm simulations. Using an LFO83 scheme they showed that even in a tropical atmosphere, greater average (and maximum) rainfall rates and less expansive precipitation areas result with N4ρ9 qh parameters than the same LFO83 scheme with N6ρ4 parameters for isolated tropical cloud clusters. They attributed this lesser accumulated rainfall primarily to the slower qh fall speed for N6ρ4, consistent with the work herein.

More recently, in agreement with the work herein, van den Heever and Cotton (2004, hereafter VC04) single-moment RAMS supercell simulations show that distributions weighted toward small graupel are associated with smaller qh aloft, initially stronger updrafts, and a smaller amount of qh ground accumulation. (RAMS users typically prescribe the qh distribution with D_{nh} instead of n_{oh}.) In contrast, however, the VC04 simulations show that those cases weighted toward the smallest graupel have cold outflow occurring earlier and are coincident with stronger low-level downdrafts than simulations herein. In their small-graupel case, more qh is able to reach ground, however. Therefore qh contributes more to the low-level downdraft and cold pool via melting and evaporation. This difference in cold pool behavior between the RAMS single-moment scheme and SAM 3-ICE may simply be due to the large differences in the respective thermodynamic and wind shear profiles used. However, other potentially large differences have been identified between the RAMS single-moment scheme and the SAM 3-ICE scheme and are under investigation: the evaporation rate equation, the species distribution prescription (prescribing D_{nh} instead of n_{oh}), and the resulting distribution fall speeds.

6. Conclusions

Using a simple liquid-ice microphysics scheme, we have shown that the amount of ground-accumulated precipitation produced by a system of simulated midlatitude multicell and supercell storms varies by a factor of about 3 or 4 (with half-circle hodograph arc lengths of 30 or 50 m s^{-1}, respectively) because of variations in the particle parametric variables describing the hail/graupel (qh) category. When only multicells are simulated (20 m s^{-1} arc length hodograph), the difference is about a factor of 2. Some treatments resulted in large and damaging hail (reaching ground) while other treatments resulted in no hail. Model treatments were based upon varying the qh particle density and intercept parameter over the ranges reported in the literature for observed midlatitude hailstorms. Smaller variations in accumulated precipitation and hail size were found for equivalent magnitude changes in the rain and snow intercept parameters. The large possible variations in the preset particle parametric variables represent an inherent uncertainty in the microphysics scheme. This uncertainty is present in similar single-moment microphysics schemes that are used within the Weather Research and Forecasting (WRF) model, Advanced Regional Prediction System (ARPS), and Regional Atmospheric Modeling System (RAMS).

Changes in the intercept parameter for the qh distribution causes changes in the qh fall velocity as well as many of the microphysical mass growth and loss rate equations for qh. As one moves toward a graupel regime (larger intercept and/or smaller particle density for qh, the qh mass growth rates increase and maximum updraft speeds increase from greater latent heating. However, despite greater net qh production rates, the smaller qh fall velocity results in larger upward qh fluxes and smaller downward qh fluxes. The smaller downward fluxes allow qh to be spread over a larger area after leaving the updraft, and less precipitation reaches ground over the 2-h integration. Storms in a graupel-weighted regime also have initially weaker near-surface downdrafts and initially warmer low-level outflow than in a hail-weighted regime. The coldest time-averaged low-level outflow are found for the original Lin et al. (1983) qh parameters with slightly (much) warmer time-averaged outflow when weighted toward larger hail (smaller graupel). Future work is needed to test if these conclusions regarding precipitation accumulations and latent heating/cooling still hold for different environments, different types of storm systems, and longer model integrations.

Because of the large inherent uncertainty in specifying the particle parametric variables and resulting precipitation uncertainty, we do not advocate the use of such three-class ice microphysics schemes or any LFO83-like scheme in cloud-scale precipitation forecasting. Understanding these large sensitivities, however, is an important first step in motivating the study and use of more sophisticated ice microphysics schemes that may have less inherent uncertainty [such as those described in Ferrier (1994), Meyers et al. (1997), and Straka and Mansell (2004, manuscript submitted to *J. Appl. Meteor.*)].

Acknowledgments. We would like to thank Drs. Jack Kain, Jason Knievel, Ted Mansell, Jeff Trapp, Morris Weisman, and the anonymous reviewers for their sage suggestions, improving an earlier draft. We have benefited from discussions with Drs. Lou Wicker, Wojciech Grabowski, and Sue van den Heever. We also benefited from questions and comments provided by audience members when this work was presented at the NSSL seminar (October 2001), fall AGU meeting (December 2001), NCAR/MMM informal and formal seminars (July 2001 and February 2002), and NWP conference (August 2002). We thank Bob Henson for providing assistance in technical editing. This research was supported by the National Science Foundation under the following grants: ATM-0003869, ATM-9617318, and ATM-9986672. Partial funding for this research was provided by the National Severe Storms Laboratory under NOAA–OU Cooperative Agreements NA67RJ0150 and NA17RJ1227.

APPENDIX

List of Microphysical Process Rates

TABLE A1. Alphabetical listing of the microphysical process rates used in the model and corresponding to the legends in Figs. 6 and 7. The second (last) letter in the name represents the species experiencing the gain (loss). To reduce ambiguity, an extra letter is included in the name (in the third letter position) to represent the accreting species when it differs from the gain species for three-body interactions. Most three-body interactions have two separate gain species. Processes associated with no phase change are checked in the last column.

Rate of change process notation (kg kg^{-1}s^{-1})	Name used in GSR2004 if different	Type of process	No phase change
qhaci		Accretion	√
qhacr		Freezing via accretion	
qhacs		Accretion	√
qhacw		Freezing via accretion	
qhcns		Aggregation	√
qhdpv		Deposition	
qhfzr		Freezing (Biggs)	
qhiacr	qiacr	Freezing via accretion (qr $\geq$ 0.1 g kg^{-1})	
qhraci	qraci	Freezing via accretion (qr $\geq$ 0.1 g kg^{-1})	
qhracs	qracs	Freezing via accretion (qr or qs $\geq$ 0.1 g kg^{-1})	
qhsacr	qsacr	Freezing via accretion (qr or qs $\geq$ 0.1 g kg^{-1})	
qhwtr	qhwet	Freezing via accretion (during wet growth)	
qidpv		Deposition	
qidpv-qvsbi		Net deposition	
qifzw		Freezing (homogeneous)	
qiint		Deposition via initiation	
qracw		Accretion	√
qrcnw		Autoconversion	√
qrhaci	qhaci	Melting via accretion ($T \geq 0$°C)	
qrhacr	qhacr	Shedding via accretion (no net transfer)	√
qrhacs	qhacs	Melting via accretion ($T \geq 0$°C)	
qrhacw	qhacw	Shedding via accretion	√
qrmlh		Melting	
qrmls		Melting	
qrsacw	qsacw	Melting via accretion by qs ($T \geq 0$°C)	
qsaci		Accretion	√
qsacr		Freezing via accretion (qr and qs < 0.1 g kg^{-1})	
qsacw		Freezing via accretion ($T < 0$°C)	
qscni		Aggregation	√
qsdpv		Deposition	
qsfi		Conversion via Bergeron	√
qsfw		Freezing via Bergeron	
qsiacr	qiacr	Freezing via accretion by qi (qr < 0.1 g kg^{-1})	
qsraci	qraci	Freezing via accretion by qr (qr < 0.1 g kg^{-1})	
qvevr		Evaporation	
qvevw		Evaporation	
qvsbh		Sublimation	
qvsbi		Sublimation	
qvsbs		Sublimation	
qwcdv		Condensation	
qwcdv-qvevw		Net condensation	
qwmli		Melting	

REFERENCES

Anderson, J. R., K. K. Droegemeier, and R. B. Wilhelmson, 1985: Simulation of the thunderstorm subcloud environment. Preprints, *14th Conf. on Severe Local Storms*, Indianapolis, IN, Amer. Meteor. Soc., 147–150.

Bennetts, D. A., and F. Rawlins, 1981: Parameterization of the ice phase in a model of midlatitude cumulonimbus convection and its influence on the simulation of cloud development. *Quart. J. Roy. Meteor. Soc.*, **107,** 477–502.

Braham, R. R., Jr., 1990: Snow particle size spectra in lake effect snows. *J. Appl. Meteor.*, **29,** 200–207.

Brooks, H. E., and R. B. Wilhelmson, 1992: Numerical simulation of a low-precipitation supercell thunderstorm. *Meteor. Atmos. Phys.*, **49,** 3–17.

Carpenter, R. L., Jr., K. K. Droegemeier, and A. M. Blyth, 1998: Entrainment and detrainment in numerically simulated cumulus congestus clouds. Part I: General results. *J. Atmos. Sci.*, **55,** 3417–3432.

Changnon, S. A., Jr., 1971: Hailfall characteristics related to crop damage. *J. Appl. Meteor.*, **10,** 270–274.

——, 1977: The scales of hail. *J. Appl. Meteor.*, **16,** 626–648.

——, 1999: Data approaches for determining hail risk in the contiguous United States. *J. Appl. Meteor.*, **38,** 1730–1739.

——, 2001: *Thunderstorms across the Nation: An Atlas of Storms, Hail, and Their Damages in the 20th Century*. Printec Press, 93 pp. [Available from Changnon Climatologist, 801 Buckthorn, Mahomet, IL 61853.]

Cheng, L., M. English, and R. Wong, 1985: Hailstone size distributions and their relationship to storm thermodynamics. *J. Climate Appl. Meteor.,* **24,** 1059–1067.

Chorin, A. J., 1967: A numerical method for solving incompressible viscous flow problems. *J. Comput. Phys.,* **2,** 12–26.

Collins, G. F., and G. Howe, 1964: Weather and extended coverage. Travelers Research Corp., Hartford, CT, 68 pp. [Available from the Illinois State Water Survey, 2204 Griffith Dr., Champaign, IL 61820-7495.]

Cotton, W. R., M. A. Stephens, T. Nehrkorn, and G. J. Tripoli, 1982: Colorado State University three-dimensional cloud/mesoscale model—1982. Part. 2, An ice phase parameterization. *J. Rech. Atmos.,* **16,** 295–320.

Dennis, A. S., P. L. Smith Jr., G. A. P. Peterson, and R. D. McNeil, 1971: Hailstone size distributions and equivalent radar reflectivity factors computed from hailstone momentum records. *J. Appl. Meteor.,* **10,** 79–85.

Droegemeier, K. K., and Coauthors, 2000: Hydrological aspects of weather prediction and flood warnings: Report of the ninth prospectus development team of the U.S. Weather Research Program. *Bull. Amer. Meteor. Soc.,* **81,** 2665–2680.

Farley, R. D., and H. D. Orville, 1986: Numerical modeling of hailstorms and hailstone growth. Part I: Preliminary model verification and sensitivity tests. *J. Climate Appl. Meteor.,* **25,** 2014–2035.

Federer, B., and A. Waldvogel, 1975: Hail and raindrop size distributions from a Swiss multicell storm. *J. Appl. Meteor.,* **14,** 91–97.

Ferrier, B. S., 1994: A double-moment multiple-phase four-class bulk ice scheme. Part I: Description. *J. Atmos. Sci.,* **51,** 249–280.

——, W.-K. Tao, and J. Simpson, 1995: A double-moment multiple-phase four-class bulk ice scheme. Part II: Simulations of convective storms in different large-scale environments and comparisons with other bulk parameterizations. *J. Atmos. Sci.,* **52,** 1001–1033.

Fovell, R. G., and Y. Ogura, 1988: Numerical simulation of a midlatitude squall line in two dimensions. *J. Atmos. Sci.,* **45,** 3846–3879.

Gilmore, M. S., J. M. Straka, and E. N. Rasmussen, 2002: Quantitative precipitation in simulated deep convection: Sensitivity to the hail/graupel category. Preprints, *15th Conf. on Numerical Weather Prediction,* San Antonio, TX, Amer. Meteor. Soc., 139–142.

——, ——, and ——, 2004: Precipitation and evolution sensitivity in simulated deep convective storms: Comparisons between liquid-only and simple ice and liquid phase microphysics. *Mon. Wea. Rev.,* **132,** 1897–1916.

Gunn, K. L. S., and J. S. Marshall, 1958: The distribution with size of aggregate snowflakes. *J. Meteor.,* **15,** 452–461.

Heymsfield, A. J., A. Bansemer, P. R. Field, S. L. Durden, J. Stith, J. E. Dye, W. Hall, and T. Grainger, 2002a: Observations and parameterizations of particle size distributions in deep tropical cirrus and stratiform clouds: Results from in situ observations in TRMM field campaigns. *J. Atmos. Sci.,* **59,** 3457–3491.

——, ——, S. Lewis, J. Iaquinta, M. Kajikawa, C. Twohy, and M. R. Poellot, 2002b: A general approach for deriving the properties of cirrus and stratiform ice cloud particles. *J. Atmos. Sci.,* **59,** 3–29.

Houze, R. A., Jr., P. V. Hobbs, P. H. Herzegh, and D. B. Parsons, 1979: Size distributions of precipitation particles in frontal clouds. *J. Atmos. Sci.,* **36,** 156–162.

Johnson, D. E., P. K. Wang, and J. M. Straka, 1993: Numerical simulations of the 2 August 1981 CCOPE supercell storm with and without ice microphysics. *J. Appl. Meteor.,* **32,** 745–759.

——, ——, and ——, 1994: A study of microphysical processes in the 2 August 1981 CCOPE supercell storm. *Atmos. Res.,* **33,** 93–123.

Kessler, E., III, 1969: *On the Distribution and Continuity of Water Substance in Atmospheric Circulation. Meteor. Monogr.,* No. 32, Amer. Meteor. Soc., 84 pp.

Klemp, J. B., and R. B. Wilhelmson, 1978: The simulation of three-dimensional convective storm dynamics. *J. Atmos. Sci.,* **35,** 1070–1096.

Knight, C. A., W. A. Cooper, D. W. Breed, I. R. Paluch, P. L. Smith, and G. Vali, 1982: Microphysics. *Hailstorms of the Central High Plains,* C. Knight and P. Squires, Eds., Vol. 1, Colorado Associated University Press, 151–193.

Lin, Y.-L., R. D. Farley, and H. D. Orville, 1983: Bulk parameterization of the snow field in a cloud model. *J. Climate Appl. Meteor.,* **22,** 1065–1092.

Liu, Y., D.-L. Zhang, and M. K. Yau, 1997: A multiscale numerical study of Hurricane Andrew (1992). Part I: Explicit simulation and verification. *Mon. Wea. Rev.,* **125,** 3073–3093.

Macklin, W. C., 1961: Accretion in mixed clouds. *Quart. J. Roy. Meteor. Soc.,* **87,** 413–424.

——, and B. F. Ryan, 1962: On the formation of spongy ice. *Quart. J. Roy. Meteor. Soc.,* **88,** 548–549.

——, and ——, 1965: The structure of ice grown in bulk supercooled water. *J. Atmos. Sci.,* **22,** 452–459.

Marécal, V., D. Hauser, and F. Roux, 1993: The 12/13 January 1988 narrow cold-frontal rainband observed during MFDP/FRONTS 87. Part II: Microphysics. *J. Atmos. Sci.,* **50,** 975–998.

Marshall, J. S., and W. M. Palmer, 1948: The distribution of raindrops with size. *J. Meteor.,* **5,** 165–166.

Marshall, T. P., R. F. Herzog, S. J. Morrison, and S. R. Smith, 2002: Hail damage threshold sizes for common roofing materials. Preprints, *21st Conf. on Severe Local Storms,* San Antonio, TX, Amer. Meteor. Soc., 95–98.

McCumber, M., W.-K. Tao, J. Simpson, R. Penc, and S. T. Soong, 1991: Comparison of ice-phase microphysical parameterization schemes using numerical simulations of tropical convection. *J. Appl. Meteor.,* **30,** 985–1004.

McFarquhar, G. M., and R. A. Black, 2004: Observations of particle size and phase in tropical cyclones: Implications for mesoscale modeling of microphysical processes. *J. Atmos. Sci.,* **61,** 422–439.

Meyers, M. P., R. L. Walko, J. Y. Harrington, and W. R. Cotton, 1997: New RAMS cloud microphysics parameterization. Part II: The two-moment scheme. *Atmos. Res.,* **45,** 3–39.

Michalakes, J., S. Chen, J. Dudhia, L. Hart, J. Klemp, J. Middlecoff, and W. Skamarock, 2001: Development of a next-generation regional weather research and forecast model. *Developments in Teracomputing,* W. Zweiflhofer and N. Kreitz, Eds., World Scientific, 269–276. [Available online at http://wrf-model.org/documentation_main.html.]

Miller, L. J., J. D. Tuttle, and C. A. Knight, 1988: Airflow and hail growth in a severe Northern High Plains supercell. *J. Atmos. Sci.,* **45,** 736–762.

Moller, A. R., C. A. Doswell III, M. P. Foster, and G. R. Woodall, 1994: The operational recognition of supercell thunderstorm environments and storm structures. *Wea. Forecasting,* **9,** 327–347.

Ovrille, H. D., and F. J. Kopp, 1977: Numerical simulation of the life history of a hailstorm. *J. Atmos. Sci.,* **34,** 1596–1618.

Pflaum, J. C., and H. R. Pruppacher, 1979: Wind tunnel investigation of the growth of graupel initiated from frozen drops. *J. Atmos. Sci.,* **36,** 680–689.

Proctor, F. H., 1988: Numerical simulations of an isolated microburst. Part I: Dynamics and structure. *J. Atmos. Sci.,* **45,** 3137–3160.

——, 1989: Numerical simulations of an isolated microburst. Part II: Sensitivity experiments. *J. Atmos. Sci.,* **46,** 2143–2165.

Pruppacher, H. R., and J. D. Klett, 1978: *Microphysics of Clouds and Precipitation.* D. Reidel, 714 pp.

Smith, J. A., M. L. Baeck, Y. Zhang, and C. A. Doswell III, 2001: Extreme rainfall and flooding from supercell storms. *J. Hydrometeor.,* **2,** 469–489.

Smith, P. L., C. G. Meyers, and H. D. Orville, 1975: Radar reflectivity

factor calculations in numerical cloud models using bulk parameterization of precipitation. *J. Appl. Meteor.,* **14,** 1156–1165.
Spahn, J. F., 1976: The airborne hail disdrometer: An analysis of its 1975 performance. Rep. 76-13, Institute of Atmospheric Sciences, South Dakota School of Mines and Technology, Rapid City, SD, 65 pp.
Straka, J. M., and J. R. Anderson, 1993: Numerical simulations of microburst-producing storms: Some results from storms observed during COHMEX. *J. Atmos. Sci.,* **50,** 1329–1348.
Tao, W.-K., and J. Simpson, 1989: Modeling study of a tropical squall-type convective line. *J. Atmos. Sci.,* **46,** 177–202.
——, and ——, 1993: Goddard cumulus ensemble model. Part I: Model description. *Terr. Atmos. Oceanic Sci.,* **4,** 35–72.
Ulbrich, C. W., 1983: Natural variations in the analytical form of the raindrop-size distribution. *J. Climate Appl. Meteor.,* **22,** 1764–1775.
van den Heever, S., and W. R. Cotton, 2004: The impact of hail size on simulated supercell storms. *J. Atmos. Sci.,* **61,** 1596–1609.
Walko, R., W. R. Cotton, M. P. Meyers, and J. Y. Harrington, 1995: New RAMS cloud microphysics parameterization. Part I. The single-moment scheme. *Atmos. Res.,* **38,** 29–62.
Weisman, M. L., and J. B. Klemp, 1984: The structure and classification of numerically simulated convective storms in directionally varying wind shears. *Mon. Wea. Rev.,* **112,** 2479–2498.
Xue, M., and Coauthors, 2001: The Advanced Regional Prediction System (ARPS)—A multiscale nonhydrostatic atmospheric simulation and prediction tool. Part II: Model physics and applications. *Meteor. Atmos. Phys.,* **76,** 134–165.
Ziegler, C. L., P. S. Ray, and N. C. Knight, 1983: Hail growth in an Oklahoma multicell storm. *J. Atmos. Sci.,* **40,** 1768–1791.